

PACS numbers: 42.55.Rz; 42.55.Xi; 78.20.Nv
DOI: 10.1070/QE2011v041n08ABEH014557

Interference study of a diode-pumped Nd : GGG active disk

G.A. Bufetova, D.A. Nikolaev, A.I. Trikshev, V.B. Tsevtkov, I.A. Shcherbakov

Abstract. **We present the results of interference studies of a diode-pumped active disk element made of a gadolinium–gallium–garnet (GGG:Nd) crystal. The disk is cut perpendicular to the crystallographic axis [001], along which the pump beam propagates. With absorbing pump radiation, a thermal lens, which has been investigated by the interference methods using linearly polarised probe radiation, is formed in the disk. At the absorbed pump power up to 12 W, the interference pattern near the disk surface is a system of concentric rings. With increasing absorbed pump power up to 24 W, the outer rings transform into hexagons. It is shown that such an interference pattern in the garnet crystal is caused by thermally induced birefringence.**

Keywords: *birefringence, disk laser.*

1. Introduction

In designing ~1-μm high-power solid-state lasers much attention is paid to the development of pumping and cooling systems. The use of a thin disk active element in such systems is one of the most successful projects aimed at overcoming the beam quality degradation caused by thermal effects in the active medium. These active elements have significant advantages over traditional rod laser due to the radiation quality and power scalability.

There are several types of disk lasers differing in the ways of pumping the active medium and in methods of heat removal from it: thin disk lasers pumped by a small diameter beam [1]; lasers with so-called active mirrors, long cavity and several active elements in the resonator pumped by a broad beam [2]; disk lasers with multichannel pump architecture [3]; cryogenically cooled lasers [4], etc. The scheme with a multichannel-pumped active medium presented in [3] is of special interest for fabricating high-power disk lasers with diffraction-limited beam divergence. The study of temperature, mechanical stress and thermal-induced birefringence distribution in the pump beam spot and in its vicinity for one channel is a necessary step in the development of this direction.

This paper presents the results of interference studies of disk active element made of gadolinium–gallium–garnet (GGG : Nd) crystal in terms of thermally induced mechanical stress and birefringence.

G.A. Bufetova, D.A. Nikolaev, A.I. Trikshev, V.B. Tsevtkov, I.A. Shcherbakov A.M. Prokhorov General Physics Institute, Russian Academy of Sciences, ul. Vavilova 38, 119991 Moscow, Russia; e-mail: bufetova@lsk.gpi.ru

Received 8 February 2011; revision received 16 May 2011
Kvantovaya Elektronika **41** (8) 681–686 (2011)
Translated by I.A. Ulitkin

2. Observation of the interference pattern near the disk surface

The experimental setup is shown in Fig. 1. The disk planes are parallel to crystallographic axes [100] and [010], and the optical axis of the scheme is parallel to the crystallographic axis [001]. A 0.808-μm diode laser with a pump beam spot diameter $d = 5$ mm is used for pumping. The thickness of the disk is $h = 2.5$ mm, and its diameter is 50 mm. The disk was attached to a water-cooled duralumin holder with a duralumin plank having a circular hole 47 mm in diameter. The thermal contact was provided using the KPT-8 thermal grease. The disk surface had a dielectric coating. The reflection coefficients of the pump from the front and rear surfaces of the disk were 0.1% and 99.6%, respectively. The pump power could be varied in the range 1–34 W. In two passes through the disk about 90% of incident radiation is absorbed. The intensity distribution in the pump beam cross section was nearly Gaussian. With absorbing pump radiation a thermal lens, which was investigated using the probe linearly polarised radiation of a 0.5435-μm He–Ne laser, was formed in the disk. The electric field vector of the probe radiation was directed along the [010] axis of the Nd:GGG crystal. The reflection coefficients of the probe radiation from the front and rear surfaces of the disk were 5% and 10%, respectively. The probe beam was directed along the normal to the disk under study and, reflecting from its two surfaces, formed an interference pattern. This pattern is similar to that with fringes of equal thickness, obtained in the presence of birefringence. The path difference of the interfering beams was equal to the optical path length of the probe radiation in the sample before pumping $P_1 = n_0 L$, and after absorption of the pump – $P_2 = (n_0 + \Delta n)(L + \Delta L)$,

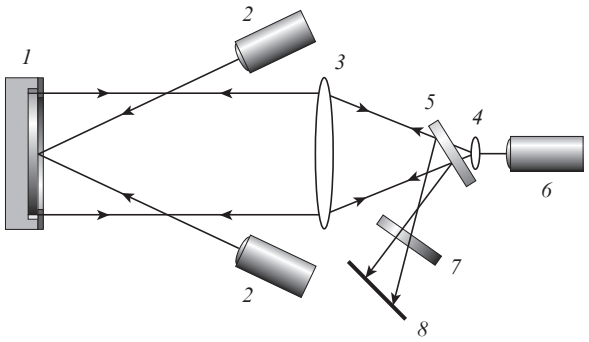

Figure 1. Optical scheme of the experiment:
(*1*) disk active element made of GGG:Nd; (*2*) diode pump system; (*3*) and (*4*) expansion telescope lenses; (*5*) beamsplitter; (*6*) He–Ne laser; (*7*) filter; (*8*) screen.

where L and n_0 are the doubled thickness and refractive index of the sample; Δn and ΔL are the changes in the refractive index and thickness L.

The interference pattern localised near the disk surface was displayed on the screen and recorded with a camera (standard recording speed of 24 fps). The camera recorded the development of the pattern upon switching on the pump and after switching it off. Processing was performed using the first frame after switching off the pump to eliminate the effect of radiation. The initial intensity distribution obtained in the absence of pumping was subtracted from the intensity distribution in this frame, so that to exclude in the difference interference pattern the phase incursion caused by the wedge shape of the disk and by the phase incursion produced due to reflection of the probe radiation from a dielectric mirror deposited on the rear side of the disk.

Below, when it comes to the interference pattern obtained in the experiment, the difference interference pattern is implied. It characterises the change in the sample temperature and induced mechanical stress, caused by to the heating during the absorption of the pump. At a small pump power (absorbed power up to 12 W) the interference pattern represented a system of concentric rings (Fig. 2a). With increasing pump power the number of rings and their radii increased. When the absorbed pump power was $W = 12$ W, we observed breaks at several points of outer interference rings. With a further increase in the pump power the outer rings transformed into hexagons (Fig. 2c). The observed interference pattern was not related to the possible asymmetry of cooling and sample mounting, because the form of the pattern did not change at different positions of the pump spot on the disk surface. At the same time by rotating the polarisation plane of the probe radiation by $\pi/2$ the interference pattern also turned by $\pi/2$, and when turning it by $\pi/4$, it transformed into a system of ellipses.

The same experimental setup (Fig. 1) was used to obtain the patterns of the depolarised component of the probe radiation, which twice passed through the disk, at different pump powers. To do this, we placed in front of the screen an additional polarisation filter (*7*) which blocked polarisation of the incident radiation. Such patterns had the fourth order rotational symmetry and the form typical of polariscopic patterns of a garnet crystal cut perpendicular to the [001] axis. Figure 3a shows the polariscopic pattern obtained at $W = 24$ W.

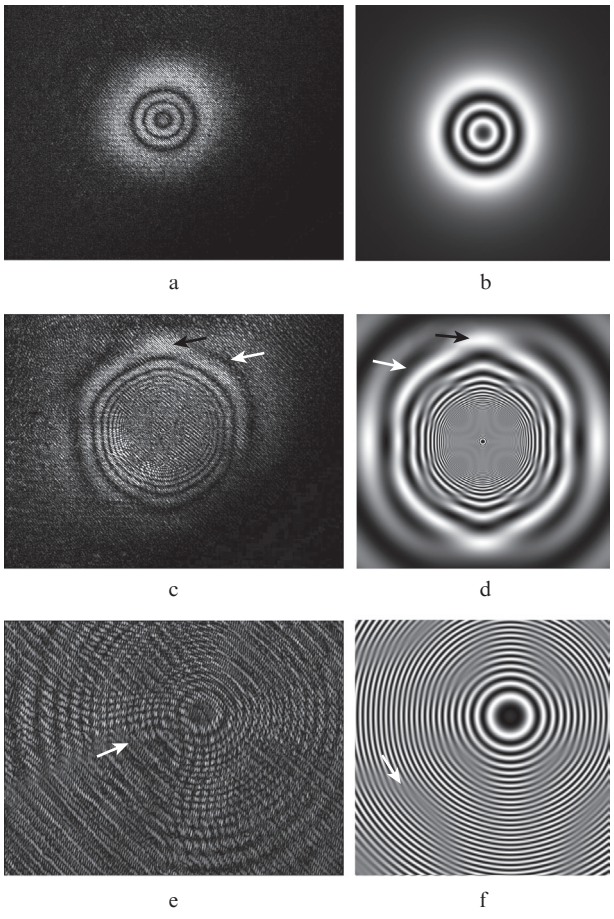

Figure 2. Experimental (a, c, e) and calculated (b, d, f) interference patterns at the absorbed pump power $W = 3$ (a, b) and 24 W (c, d), the pump spot diameter $d = 5$ mm. Figures 2e, f shows the central part of the frames from Figs 2c, d. The width of the frame in Fig. 2a corresponds to 38.9 mm, and in Fig. 2e – to 9.5 mm. Arrows indicate the characteristic features of the interference patterns (see the text).

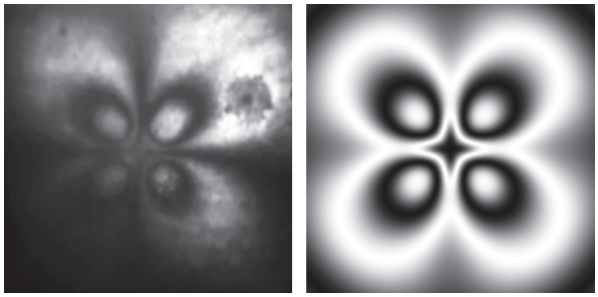

Figure 3. Experimental (a) and calculated (b) polariscopic patterns obtained at the absorbed pump power $W = 24$ W.

To our knowledge, hexagonal contours in the interference pattern near the garnet crystal surface (crystallographic axes [010] and [100] are parallel to the surface) have never been observed previously. In order to determine whether the features of such an interference pattern are due to the induced thermo-mechanical stresses in the disk, we simulated a thermal lens in the disk and the interference pattern. The problem was solved in the plane stress approximation. For an arbitrary point of the disk surface we calculated eigenpolarisations and corrections to the refractive index. Then, we calculated the square of the field strength (proportional to the intensity) of the interfering probe radiation at this point, and then compared the calculated and experimental interference patterns. Unlike previous similar calculations for disk active elements (see, for example, [4]), in our case we used experimental (averaged over the disk thickness) data on the temperature distribution along the disk surface (see Section 4) rather than computational.

In calculations we used the following physical characteristics of the GGG crystal: $\beta = 17.5\times10^{-6}$ K^{-1}, the temperature coefficient of refractive index [5]; $\mathcal{E} = 2.25\times10^{11}$ Pa, Young's modulus [6]; $\nu = 0.28$, Poisson's ratio [6]; $n_0 = 1.98$ (at a wavelength of 0.5461 μm); $p_{11} = -0.086$, $p_{12} = -0.027$, $p_{44} = -0.078$, elastooptical coefficients [6]; $\xi = 2p_{44}/(p_{11} - p_{12}) = 2.64$, the optical anisotropy parameter; $\alpha_T = 8\times10^{-6}$ K^{-1}, the linear expansion coefficient [5]. We also used the notations: σ_{ij}, ε_{ij}, components of stress and strain tensors in the crystallographic

system of coordinates ($i,j = 1,2,3$); B_{ij}, the components of the dielectric impermeability tensor; ΔB_{ij}, the components of the change in the dielectric impermeability tensor.

3. Calculation of the interference pattern near the disk surface

To calculate the light intensity in the interference pattern near the disk surface, we calculated projections of the electric field onto the directions of eigenpolarisations for an arbitrary point on the surface, and defined the field intensities of the probe radiation.

In the calculations we used three systems of coordinates (Fig. 4). Position of the points on the disk surface was specified in the cylindrical coordinate system $\boldsymbol{r},\varphi,z$, whose origin was associated with the pump spot centre on the disk surface ($z = 0$). Elastooptical coefficients of the crystal were given in the crystallographic coordinate system with axes $x \| [100]$, $y \| [010]$, $z \| [001]$. In addition, the local coordinate system with axes directed along eigenpolarisations at a given point of the crystal was tied to each point of the disk surface. The directions of eigenpolarisations coincide with the principal directions of the change in the dielectric impermeability tensor ΔB.

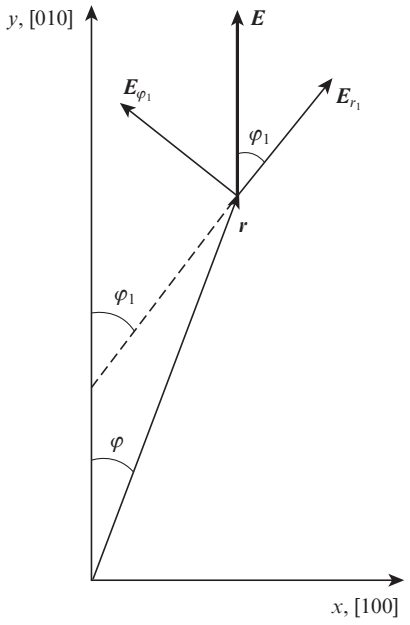

Figure 4. Coordinate system used in this paper (see the text).

The pump spot diameter (d = 5 mm) was significantly smaller than the disk diameter, and the temperature distribution in the plane of the disk was axially symmetric. Nonuniform temperature distribution resulted in the thermal stresses in the crystal and lead to birefringence. The incident wave of the probe radiation passing through each point of the heated region cross section can be decomposed into two components with field strengths $\boldsymbol{E}_{r_1}$ and $\boldsymbol{E}_{\varphi_1}$, directed along the eigenpolarisations at a given point of the crystal. The direction of the vector $\boldsymbol{E}_{r_1}$ is closer to the radial and the direction of the vector $\boldsymbol{E}_{\varphi_1}$ – to the tangential direction in the above-mentioned cylindrical coordinate system. Therefore, in what follows, $\boldsymbol{E}_{r_1}$ is called the radial field component, and $\boldsymbol{E}_{\varphi_1}$ – tangential. Waves with strengths $\boldsymbol{E}_{r_1}$ and $\boldsymbol{E}_{\varphi_1}$ spread at different velocities.

The electric field vector of the incident wave $\boldsymbol{E}$ in the local coordinate system can be decomposed into the components (Fig. 4)

$$\begin{aligned} \boldsymbol{E}_{r_1} &= \boldsymbol{E}\cos\varphi_1\cos(\omega t), \\ \boldsymbol{E}_{\varphi_1} &= \boldsymbol{E}\sin\varphi_1\cos(\omega t), \end{aligned} \tag{1}$$

where φ_1 is the angle between the direction of the incident probe radiation polarisation (in our case – along the [010] axis) and the direction of the vector $\boldsymbol{E}_{r_1}$. The angle φ_1 differs from the polar angle φ; these angles are related by the expression [7]

$$\tan 2\varphi_1 = \xi \tan 2\varphi\,. \tag{2}$$

The probe radiation has only a radial component of the field $\boldsymbol{E}_{r_1}$ for points in the pump spot which are located along the y axis ($\varphi = \varphi_1 = 0$), and only a tangential component of the field $\boldsymbol{E}_{\varphi_1}$ along the x axis ($\varphi = \varphi_1 = \pi/2$). At other points the vector $\boldsymbol{E}$ will have non-zero components $\boldsymbol{E}_{r_1}$ and $\boldsymbol{E}_{\varphi_1}$.

After two passes through the disk, each of these components takes an additional phase incursion ψ_{r_1} or ψ_{φ_1}. Near the disk surface the total field is determined by the field $\boldsymbol{E}$ of the wave reflected from the front surface and by the field $\boldsymbol{E}'$ of the wave passing through the disk and reflected from its rear surface. We assume for simplicity that the intensity of waves reflected from two surfaces of the disk are equal, then the radial and tangential components of the total field in the local coordinate system are written in the form:

$$\begin{aligned} \boldsymbol{E}_{r_1} + \boldsymbol{E}'_{r_1} &= \boldsymbol{E}\cos\varphi_1[\cos(\omega t) + \cos(\omega t + \psi_{r_1})], \\ \boldsymbol{E}_{\varphi_1} + \boldsymbol{E}'_{\varphi_1} &= \boldsymbol{E}\sin\varphi_1[\cos(\omega t) + \cos(\omega t + \psi_{\varphi_1})], \end{aligned} \tag{3}$$

where the phases ψ_{r_1} and ψ_{φ_1} are the functions of the coordinates r and φ of the given point on the disk surface. Then the square of the field strength at a point can be expressed in terms of the radius r and the polar angle φ with account for relation (2). After its time-averaging, we obtain

$$\begin{aligned} E^2_{\Sigma}(r,\varphi) &= (E_{r_1} + E'_{r_1})^2 + (E_{\varphi_1} + E'_{\varphi_1})^2 \\ &= E^2(1 + \cos^2\varphi_1\cos\psi_{r_1} + \sin^2\varphi_1\cos\psi_{\varphi_1}). \end{aligned} \tag{4}$$

Expression (4) determines the probe radiation intensity at an arbitrary point on the disk surface. The phase incursion $\psi_{r_1,\varphi_1}(r,\varphi)$ at each point of the disk is related to the optical path difference $\Delta P_{r_1,\varphi_1}(r,\varphi)$ by the expression

$$\psi_{r_1,\varphi_1}(r,\varphi) = \Delta P_{r_1,\varphi_1}(r,\varphi)\frac{2\pi}{\lambda}, \tag{5}$$

where λ is the probe radiation wavelength. The integer part $[\Delta P_{r_1,\varphi_1}(r,\varphi)/\lambda]$ corresponds to the number N of the maximum (or bright ring) in the interference pattern.

4. Calculation of the optical path length of the probe radiation in the disk

The experimentally observed interference pattern at each point near the disk surface was determined by the optical path difference of the beam reflected from the front surface, and the

beam passing through the disk and reflected from its rear surface. When passing through the disk the probe radiation intersected regions with different temperatures, because the temperature over the disk thickness was not constant. Therefore, the interference pattern was determined by the phase incursion, integral over the disk thickness, and this phase incursion could be used to find a phase profile averaged over the disk thickness.

In calculatying thermal stresses in the disk it is needed to know the temperature distribution $T(r)$. In some cases, when determining the temperature profile in axially symmetric active elements, use can be made of analytic solutions of a two-dimensional heat equation for a thin plate or a cylinder [4, 5]. In our experiments, the heat problem is not reduced to any of these approximations, because the disk thickness and the pump spot diameter are close quantities.

We determined the distribution $T(r)$ in another way – by the interference pattern, suggesting that the main contribution to the phase incursion for an arbitrary point on the surface is made by terms proportional to the temperature at this point. In the calculations we assumed that the distribution function $T(r)$ coincides with the normalised distribution function of the phase incursion, multiplied by the maximum temperature which was found from the condition of equality of the number of interference maxima in theoretical and experimental interference patterns. The temperature distribution in the sample was axially symmetric which was due to the disk pumping and cooling geometries and was confirmed by the form the interference pattern. Figure 5 shows the polarisation averaged profiles of the phase incursion (number of rings), measured by the experimental interference patterns shown in Figs 3a, c, e. For the outer rings the average value of their radius was selected.

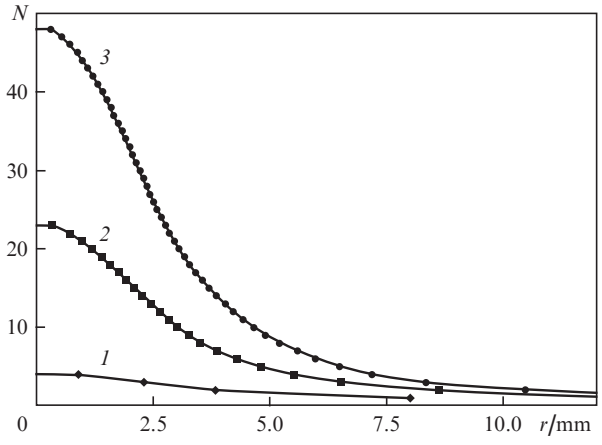

Figure 5. Ring number N in the interference pattern as a function of radius for the absorbed pump power $W = 3$ (*1*), 12 (*2*) and 24 W (*3*).

Because the linear dimensions of the disk surface and the diameter of the interference rings are much larger than the disk thickness, in calculating the thermal stresses we used the plane stress approximation [8] and neglected for simplicity the change in the temperature gradient in the disk along the z axis, because the mechanical stresses in the object in the direction of the constant temperature gradient do not arise [7].

At a given temperature distribution the tensor components of stress (σ), strain (ε) and displacement (u) at each point in the crystal are determined by the equilibrium equations, relationships between strains and displacements, strains and stresses, and boundary conditions. The corresponding equations are given in [9]. For a thin plate the stress components along the z axis are equal to zero in the plane stress approximation: $\sigma_{zz} = \sigma_{rz} = \sigma_{\varphi z} = 0$. In this case, the stress and strain depend on two variables – r and φ – in the sample plane.

As a result of pumping up to terms of the second order smallness, the change (measured by the interference pattern) in the optical path of the probe radiation in the sample is expressed as:

$$\Delta P = P_2 - P_1 = L\Delta n + n_0\Delta L = L(\Delta n + n_0\varepsilon_{zz}), \tag{6}$$

where Δn are the refractive index changes caused by temperature and mechanical stresses [7]; the term $n_0\varepsilon_{zz}$ takes into account the elongation of the active element.

As a result of the induced birefringence, the optical path lengths for radially and tangentially polarised light are different. At each point of the disk surface, there are two components of the change in optical path length ($\Delta P_{r_1,\varphi_1}$), which can be expressed through the change in the principal values of the optical indicatrix $\Delta B_{r_1,\varphi_1}(r,\varphi)$:

$$\Delta P_{r_1,\varphi_1} = L\left(\beta T + n_0\varepsilon_{zz} - \frac{n_0^3}{2}\Delta B_{r_1,\varphi_1}\right), \tag{7}$$

where the first term takes into account the temperature changes in the refractive index, the second term – thermal expansion, and the third term – the contribution of thermal stresses into the refractive index change.

In the calculations we used the methods described in [7–10]. For an Nd:GGG crystal the tensor components of the elasto-optic coefficients p_{11}, p_{12}, p_{44} are given in the crystallographic coordinate system [6]. Taking into account the geometry of the problem, the stress tensor is more convenient to write in the cylindrical coordinate system. Because the calculations should be performed in one coordinate system, the relations between the tensor components ΔB_{ij}, ε_{ij} and σ_{ij} were written in the crystallographic system. Then, the eigenvalues ΔB_{r_1} and ΔB_{φ_1} were expressed via ΔB_{ij}, and the components σ_{ij} – via eigenvalues σ_r and σ_φ and the angle φ (the angle of the main direction of the tensor σ). As a result, we derived the expressions for $\Delta B_{r_1,\varphi_1}(r,\varphi)$, which are convenient for further calculations.

Expressions for the radial and tangential stress components that are the principal values of the stress tensor at the point with coordinates r, φ in the case of a plane axially symmetric thermal field in the cylindrical coordinate system have the form [8]

$$\sigma_r = \frac{\alpha_T \mathcal{E}}{2}(T_R - T_r),\ \sigma_\varphi = \frac{\alpha_T \mathcal{E}}{2}[T_R + T_r - 2T(r)], \tag{8}$$

where T_R is the average temperature of the disk of radius R; T_r is the average temperature inside the disk bounded by a circle of radius r:

$$T_r = \frac{2}{r^2}\int_0^r T(r)\,r\,\mathrm{d}r. \tag{9}$$

Expressions for ΔB_{r_1} and ΔB_{φ_1} can be written in the form:

$$\Delta B_{r_1,\varphi_1}(r,\varphi) = \frac{1}{2}\left\{\frac{\sigma_r+\sigma_\varphi}{\mathcal{E}}[p_{11}(1-\nu) + p_{12}(1-3\nu)] + 2\alpha_T T(r)(p_{11}+2p_{12})\right\} \pm \frac{1}{2}\left\{\frac{1+\nu}{\mathcal{E}}(\sigma_r-\sigma_\varphi)(p_{11}-p_{12})\sqrt{\frac{1+\xi^2\tan^2(2\varphi)}{1+\tan^2(2\varphi)}}\right\}. \quad (10)$$

As a result, components (7) can be written as

$$\Delta P_{r_1,\varphi_1}(r,\varphi) = L\left\{T(r)\left[\beta + \alpha_T n_0 - \alpha_T\frac{n_0^3}{4}(p_{11}+2p_{12})\right] + [T(r)-T_R]\alpha_T\left\{\frac{n_0^3}{4}[p_{11}(1-\nu)+p_{12}(1-3\nu)] + \nu n_0\right\} \pm [T_r - T(r)]\alpha_T\frac{n_0^3}{4}(1+\nu)(p_{11}-p_{12})\sqrt{\frac{1+\xi^2\tan^2(2\varphi)}{1+\tan^2(2\varphi)}}\right\}. \quad (11)$$

We select in (11) the terms depending only on the radius r. Then, the phase incursion component, which is common for both eigenpolarisations, has the form

$$\psi_0(r) = \frac{2\pi}{\lambda}L\left\{T(r)\left[\beta + \alpha_T n_0 - \alpha_T\frac{n_0^3}{4}(p_{11}+2p_{12})\right] + [T(r)-T_R]\alpha_T\left\{\frac{n_0^3}{4}[p_{11}(1-\nu)+p_{12}(1-3\nu)] + \nu n_0\right\}\right\}, \quad (12)$$

and the phase incursion $\Delta\psi(r,\varphi)$, which depends on the radius r, polar angle φ and is equal to the phase difference for eigenpolarisations, has the form

$$\Delta\psi(r,\varphi) = \frac{2\pi}{\lambda}L[T_r - T(r)]\alpha_T\frac{n_0^3}{4}(1+\nu)(p_{11}-p_{12}) \times\sqrt{\frac{1+\xi^2\tan^2(2\varphi)}{1+\tan^2(2\varphi)}}. \quad (13)$$

Then, formula (4) can be represented as follows:

$$E_\Sigma^2(r,\varphi) = E^2\{1 + \cos^2\varphi_1\cos[\psi_0(r)+\Delta\psi(r,\varphi)] + \sin^2\varphi_1\cos[\psi_0(r)-\Delta\psi(r,\varphi)]\}. \quad (14)$$

Our calculations are valid for any crystal with a garnet structure.

Substitution of the numerical parameters of the Nd : GGG crystal in (11) makes it possible to evaluate the contribution of individual terms into the phase incursion (Fig. 6):

$$\frac{\Delta P_{r_1,\varphi_1}(r,\varphi)}{\lambda} \approx 10^{-2}\left\{35T(r) + 3.1[T(r)-T_R] \pm 1.1[T_r - T(r)]\sqrt{\frac{1+2.64^2\tan^2(2\varphi)}{1+\tan^2(2\varphi)}}\right\}. \quad (15)$$

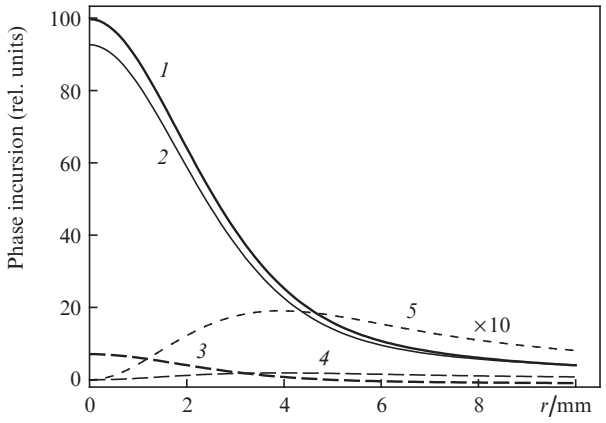

Figure 6. Distribution function of the phase incursion $\Delta P_{r_1}(r,\varphi)$ (*1*), as well as the contribution of terms proportional to $T(r)$ (*2*), $T(r)-T_R$ (*3*), $T_r - T(r)$ (*4*,*5*) at $\varphi = \pi/4$.

One can see that the phase incursion profile [curve (*1*)] is almost completely determined by the temperature profile [curve (*2*)]; therefore, the choice of approximation of the temperature function by the phase incursion profile seems justified. Note [see expression (8)] that the difference $\sigma_r - \sigma_\varphi$ is proportional to $T_r - T(r)$. Curve (*5*) is shown in an enlarged scale. It can be seen that the maximum difference $T_r - T(r)$ and, consequently, $\sigma_r - \sigma_\varphi$ is achieved outside the pump spot (at $r \approx 4$ mm).

It follows from (4) and (14) that the interference maxima at $\varphi = 0$ are determined by the radial component of the phase incursion ψ_{r_1}, and if $\varphi = \pi/2$ – by the tangential component ψ_{φ_1}.When $\varphi = \pi/4$, equation (14) reduces to the form that allows the difference between the phase incursions $\Delta\psi(r,\varphi)$ for the radial and tangential polarisation components to be found. Below we present formulas for determining the position of interference maxima:

$$E_\Sigma^2(r,0) = E^2\{1+\cos[\psi_0(r)+\Delta\psi(r,0)]\} \text{ at } \varphi = 0,$$
$$E_\Sigma^2(r,\pi/2) = E^2\{1+\cos[\psi_0(r)-\Delta\psi(r,\pi/2)]\} \text{ at } \varphi = \pi/2, \quad (16)$$
$$E_\Sigma^2(r,\pi/4) = E^2\{1+\cos[\psi_0(r)]\cos[\Delta\psi(r,\pi/4)]\} \text{ at } \varphi = \pi/4.$$

Figure 7 shows the function $F_1(r) = E_\Sigma^2(r,\pi/4)$ corresponding to the beat pattern. Modulating is the phase difference function of radial and tangential components $F_2(r) = E_2\{1 + \cos[\Delta\psi(r,\pi/4)]\}$.

Comparison of theoretical and experimental interference patterns (Figs 2c, d) showed good correspondence between their features: the hexagonal contour, thickening of the hexagon vertices and incomplete dark ring behind the hexagon are clearly visible. Figures 2e, f present the central part of the interference pattern with concentric rings and contours of interference lobes. The contours of the lobes can be also seen in Figs 2c, d. Against the background of the rings, we see a four-lobe contour of the change in the fringe contour corresponding to the change in the lobe colour in polariscopic patterns (Fig. 3).

Thus, the interference pattern obtained by using linearly polarised light contains information about the absolute values ψ_{r_1} and ψ_{φ_1}, as well as their difference. Comparison of the theoretical and experimental patterns (Fig. 2) suggests that these patterns have the second-order rotational symmetry, and

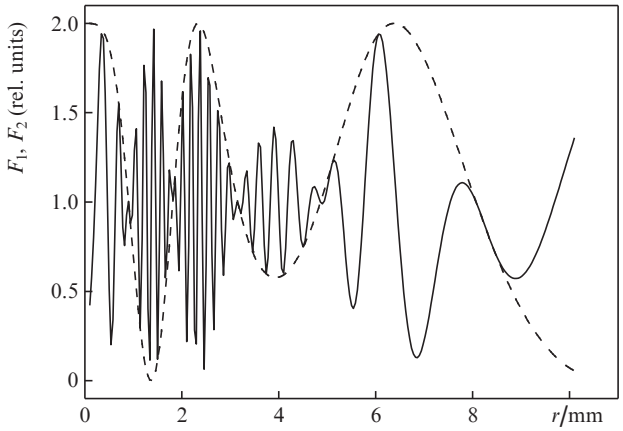

Figure 7. Function $F_1(r)$ (solid curve) and modulating function $F_2(r)$ (dashed curve).

the hexagonal contour is the result of interference of the beams of linearly polarised light in a crystal with the fourth-order rotational symmetry in the case of induced birefringence.

5. Conclusions

Comparison of experimental data and results of the calculations allows the following conclusions to be drawn.

(i) The maximum difference between the quantities σ_r and σ_φ is achieved outside the pump beam spot, approximately at a distance of its double radius. In this region the phase difference between radiations with two polarisations reaches maximum values, and the interference pattern exhibits a change in the form of the rings.

(ii) The proposed calculation model and method for estimating the temperature profile in the medium are consistent with the results of experiments.

References

1. Giesen A., Hugel H., Voss A., et al. *Appl. Phys. B*, **58**, 365 (1994).
2. Vetrovec J. *Proc. SPIE Int. Soc. Opt. Eng.*, **4270**, 45 (2001).
3. Garnov S.V., Mikhailov V.A., Serov R.V., Smirnov V.A., Tsvetkov V.B., Shcherbakov I.A. *Kvantovaya Elektron.*, **37** (10), 910 (2007) [*Quantum Electron.*, **37** (10), 910 (2007)].
4. Vyatkin A.G., Khazanov E.A. *Kvantovaya Elektron.*, **39** (9), 814 (2009) [*Quantum Electron.*, **39** (9), 814 (2009)].
5. Chénais S., Balembois F., Druon F., Lucas-Leclin G., Georges P. *IEEE J. Quantum Electron.*, **40** (9), 1235 (2004).
6. Chistyi I.L., Kitaeva V.F., Osiko V.V., Sobolev N.N., Starikov B.P., Timoshechkin M.I. *Fiz. Tverd. Tela*, **17**, 1434 (1975).
7. Mezenov A.V., Soms L.N., Stepanov A.I. *Termooptika tverdotel'nykh lazerov* (Thermooptics of Solid-state Lasers) (Leningrad: Mashinostroenie, 1986).
8. Kovalenko A.D. *Vvedenie v termouprugost'* (Introduction to Thermoelasticity) (Kiev: Naukova Dumka, 1965) p. 97.
9. Belostotsky B.R., Rubanov A.S. *Teplovoi regim opticheskikh kvantovykh generatorov* (Thermal Regime of Optical Quantum Generators) (Moscow: Energiya, 1973) p. 135.
10. Koechner W., Rice D. *IEEE J. Quantum Electron.*, **6** (9), 557 (1970).